Fundamentals of Semiconductor C-V Measurements

Tweet 0

By Lee Stauffer, Keithley Instruments, December 2008

Capacitance-voltage (C-V) testing is widely used to determine semiconductor parameters, particularly in MOSCAP and MOSFET structures. However, other types of semiconductor devices and technologies also can be characterized with C-V measurements, including bipolar junction transistors, JFETs, III-V compound devices, photovoltaic cells, MEMS devices, organic thin film transistor (TFT) displays, photodiodes, and carbon nanotubes.

The fundamental nature of these measurements makes them relevant to a wide range of applications and disciplines. They are used in the research labs of universities and semiconductor manufacturers to evaluate new materials, processes, devices, and circuits. C-V measurements are extremely important to product and yield enhancement engineers responsible for improving processes and device performance. Reliability engineers use these measurements to qualify material suppliers, monitor process parameters, and analyze failure mechanisms.

With appropriate methodologies, instrumentation, and software, a multitude of semiconductor device and material parameters can be derived. This information is used all along the production chain beginning with evaluation of epitaxially grown crystals including parameters such as average doping concentration, doping profiles, and carrier lifetimes.

In wafer processes, C-V measurements can reveal oxide thickness, oxide charges, contamination from mobile ions, and interface trap density. These measurements continue to be important after other process steps such as lithography, etching, cleaning, dielectric and polysilicon depositions, and metallization. After devices are fully fabricated on the wafer, C-V is used to characterize threshold voltages and other parameters during reliability and basic device testing and to model the performance of these devices.

The Physics of Semiconductor Capacitance

A MOSCAP structure is a fundamental device formed during semiconductor fabrication (**Figure 1**). Although these devices may be used in actual circuits, they typically are integrated into fabrication processes as test structures. Since they are simple structures and fabrication is easy to control, they are a convenient way to evaluate the underlying processes.

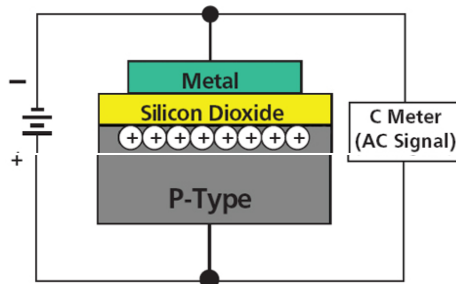

Figure 1. C-V Measurement Circuit for a MOSCAP Structure Formed on a P-Type Substrate

The metal/polysilicon layer shown in Figure 1 is one plate of the capacitor, and silicon dioxide is the insulator. Since the substrate below the insulating layer is a semiconducting material, it is not by itself the other plate of the capacitor. In effect, the majority charge carriers become the other plate.

Physically, capacitance (C) is determined from the variables in the following equation:

$$C = A\ (k/d)$$

where: A = area of the capacitor
k = dielectric constant of the insulator
d = separation of the two plates

As a result, the larger A and k are and the thinner the insulator is, the higher the capacitance will be. Typically, semiconductor capacitance values range from nanofarads to picofarads or smaller.

The procedure for taking C-V measurements involves the application of DC bias voltages across the capacitor while making the measurements with an AC signal (Figure 1). Commonly, AC frequencies from about 10 kHz to 10 MHz are used for these measurements. The bias is applied as a DC voltage sweep that drives the MOSCAP structure from its accumulation region into the depletion region and then into inversion (**Figure 2**).

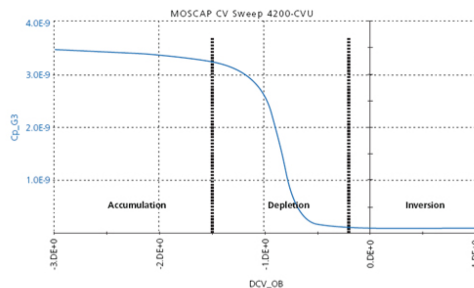

Figure 2. DC Bias Sweep of MOSCAP Structure Obtained During C-V Testing

A strong DC bias causes majority carriers in the substrate to accumulate near the insulator interface. Since they can't get through the insulating layer, capacitance is at a maximum in the accumulation region as the charges stack up near that interface because d is at a minimum (Figure 1). One of the fundamental parameters that can be derived from C-V accumulation measurements is the silicon dioxide thickness.

As the bias voltage decreases, majority carriers get pushed away from the oxide interface, and the depletion region forms. When the bias voltage is reversed, charge carriers move the greatest distance from the oxide layer, and capacitance is at a minimum because d is at a maximum. From this inversion region capacitance, the number of majority carriers can be derived. The same basic concepts apply to MOSFETs even though their physical structure and doping are more complex.

Many other parameters can be derived from the three regions shown in Figure 2 as the bias voltage is swept through them. Different AC signal frequencies can reveal additional details. Low frequencies uncover what are called quasistatic characteristics where high-frequency testing is more indicative of dynamic performance. Both types of C-V testing often are required.

Basic Test Setup

Figure 3 is the block diagram of a basic C-V measurement setup. Because C-V measurements actually are made at AC frequencies, the capacitance for the DUT is calculated with the following:

$$C_{DUT} = \frac{I_{DUT}}{2\pi f V_{AC}}$$

where: I_{DUT} = magnitude of the AC current through the DUT
f = test frequency
V_{AC} = magnitude and phase angle of the measured AC voltage

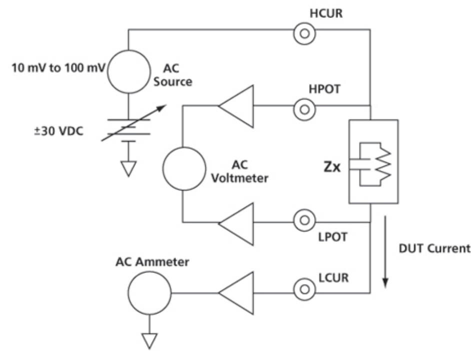

Figure 3. Basic Test Setup for C-V Measurements

In other words, the test measures the AC impedance of the DUT by applying an AC voltage and measuring the resulting AC current, AC voltage, and impedance phase angle between them.

These measurements take into account series and parallel resistance associated with the capacitance as well as the dissipation factor. **Figure 4** illustrates the basic circuit variables that can be derived from the measurements.

Z, Theta: Impedance and Phase Angle
R + jX: Resistance and Reactance
Cp–Gp: Parallel Capacitance and Conductance
Cs–Rs: Series Capacitance and Resistance

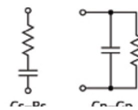

Figure 4. Basic Electrical Variables Available From C-V Measurements

Challenges of C-V Measurements

Although a block diagram of a C-V test setup looks deceptively simple, certain challenges are associated with this testing. Typically, test personnel have problems in the

following areas:
- Low-capacitance measurements of picofarads and smaller values
- C-V instrument connections through a prober to the wafer device
- Leaky, high D capacitance measurements
- Using hardware and software to acquire the data
- Parameter extractions

Overcoming these challenges requires careful attention to the techniques used along with appropriate hardware and software.

Low-Capacitance Measurements
If C is small, the DUT's AC response current is small and hard to measure. However, at higher frequencies, the DUT impedance is reduced so the current increases and is easier to measure.

Often, semiconductor capacitance is less than 1 pF, which is below the capabilities of many LCR meters. Even those claiming to measure these small capacitance values may have confusing specifications that make it difficult to determine the final accuracy in the measurement. If accuracy over the instrument's full measurement range is not explicitly stated, you need to clarify this with the manufacturer.

C-V Measurement Connections
In most test environments, the DUT is a test structure on a wafer: It is connected to the C-V instrument through a prober, a probe card adapter, and a switch matrix. Even if no switch is involved, there still is a prober and significant cabling.

At high frequencies, special corrections and compensation must be applied. Usually, this is achieved with some combination of an open, short, or calibration device.

Because of the complexity of the hardware, cabling, and compensation techniques, it is a good idea to confer with C-V test application engineers. They are skilled at working with various probe systems to overcome many types of interconnection problems.

High D (Leaky) Capacitors
In addition to having a low C value, a semiconductor capacitor also may be leaky. That is the case when the equivalent R in parallel with C is too low. This results in resistive impedance overwhelming the capacitive impedance, and the C value gets lost in the noise.

For devices with ultrathin oxide layers, D values can be greater than five. In general, as D increases, the accuracy of a C measurement is rapidly degraded so high D is a limiting factor in the practical use of a C meter. Again, higher frequencies can help solve the problem. At higher frequencies, the capacitive impedance is lower, resulting in a C current that is higher and more easily measured.

Obtaining Useful Data
In addition to accuracy issues, practical considerations in C-V data collection include the instrumentation's range of test variables, versatility of parameter extraction software, and ease of hardware usage. Traditionally, C-V testing has been limited to about 30 V and 10 mA DC bias. However, many applications such as characterizing laterally diffused MOS structures, low-k interlayer dielectrics, MEMS devices, organic TFT displays, and photodiodes require tests at higher voltage or current. For these applications, a separate high-voltage DC power supply and C meter are required; DC bias from 0 to ?400 V and a current output up to 300 mA are very useful. Being able to apply differential DC bias on both the HI and LO terminals of the C-V instrument offers more flexible control over electric fields within the DUT, which is very helpful in researching and modeling novel devices such as nanoscale components.

The instrumentation software should include ready-to-run test routines that do not require user programming. These should be available for the most widely used device technologies and test regimens.

Some researchers also may be interested in less common tests such as performing both a C-V and C-f sweep on a metal-insulator-metal capacitor, measuring small interconnect capacitance on a wafer, or doing a C-V sweep on a two-terminal nanowire device. The parameter extractions should be easily obtained with automated curve plotting.

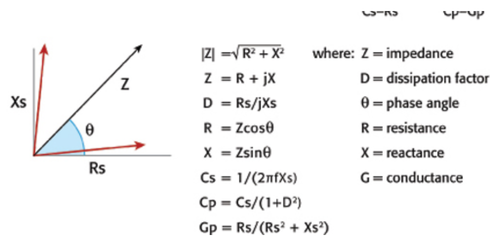

Often, engineers and researchers are expected to perform C-V measurements with little experience and training on the instrumentation. A test system with an intuitive user interface and easy-to-use features makes this practical. Simple test setup, sequence control, and data analysis are essential. Otherwise, you spend more time learning the system than collecting and using the data.

Other considerations for a test system include:
• Tightly integrated source-measure units, a digital oscilloscope, and a C-V meter
• Easy integration with other external instruments
• DC biasing down to millivolts and capacitance measurements down to femtofarads to support high-resolution, precise measurements at the probe tips
• Test setups and libraries that can be easily modified
• Diagnostic/troubleshooting tools that let you know whether or not the system is performing correctly

About the Author

Lee Stauffer is a senior marketer responsible for developing and supporting products for the semiconductor manufacturing and research markets at Keithley Instruments. His formal education in electrical engineering and semiconductor device physics is complemented by 20 years experience in semiconductor process and product engineering, device characterization, and instrumentation design. Keithley Instruments, 28775 Aurora Rd., Cleveland, OH 44139, 440-248-0400, e-mail: lstauffer@keithley.com

Predicting the *J–V* Curve in Organic Photovoltaics Using Impedance Spectroscopy

*James I. Basham, Thomas N. Jackson, and David J. Gundlach**

Impedance spectroscopy is used as a method to predict the current–voltage curve in organic photovoltaic devices. This technique allows the quantification of the recombination rate, series resistance, carrier density, and lifetime very close to normal operating conditions. The current density is reconstructed from the generation and recombination rates. Excellent agreement with measured results is observed using this simple model. The order of recombination is found to be strongly bias dependent, displaying a shift in the dominant form of recombination from trap-mediated at low carrier densities to bimolecular at high carrier densities. Mobility is shown for a range of intensities and is found to vary significantly with fabrication conditions.

1. Introduction

Organic photovoltaics show promise as a potential low-cost, efficient and scalable technology.[1,2] As such, there is great interest in developing predictive device models and quantitative metrics for device performance. Predicting the current density–voltage (*J–V*) curve is a topic of interest, as it is among the most basic device quality metrics.[3–14] The shape of the *J–V* curve is heavily influenced by recombination, and it is hoped that by understanding and reducing recombination efficiencies could be further improved. A rough first approximation of the *J–V* curve has sometimes been to add the short circuit current to either the dark *J–V* curve or a diode model using parameters extracted in the dark. However, this is not the best approach as the dark condition is very different from the illuminated condition.[15] In the dark, carriers are injected from the contacts, and may be of a single type whereas photogeneration leads to equal generation of positive and negative charges at relevant illumination conditions. The role of bimolecular recombination will change in the transition from a single carrier device to a two carrier device. The built in voltage and carrier densities and distributions also differ in the light and dark. For these reasons the curvature of the dark and illuminated *J–V* curves can be quite different. More than a simple offset is needed to relate one to the other. A much better approach is to subtract the recombination rate from the generation rate, provided that recombination is also measured under one sun illumination.[5,8] Generally speaking, it is best to make electronic measurements of solar cells at a condition as close to normal operation as possible. Carrier distribution, concentration, type, lifetime, recombination mechanism, etc. can vary widely when the same device is subjected to different bias and illumination conditions. It is not a trivial matter to ensure that a device behaves the same under measurement conditions as when used for its intended purpose.

Several transient photovoltage techniques have demonstrated the ability to measure free carrier densities and lifetimes in solar cells and can be used to reconstruct the *J–V* curve.[16–21] We demonstrate here the strengths and benefits of using impedance spectroscopy because it is quasi-steady state and can be performed at one Sun illumination. This avoids the large instantaneous fluences and potential variations required by certain transient techniques, and results in a measurement condition much closer to normal operation. The *J–V* curve can be predicted when the generation and recombination rates are known. In this work, we use impedance spectroscopy to quantify the recombination of a solar cell under one Sun illumination and a varied bias. This allows the *J–V* curve to be modeled as the generation minus recombination. We interpret carrier information from impedance spectroscopy in a way previously applied to small signal transient photovoltage measurements.[8,16] We demonstrate that bias and illumination have a strong influence on the mechanism of recombination and charge carrier mobility. We further show the effect of processing by comparing the response of a high efficiency cell made by slow drying and annealing of a poly-3-hexylthiophene (P3HT):phenyl-C_{61}-butyric acid methyl ester ($PC_{61}BM$) film (referred to as "Slow AN") to a low efficiency cell made of a fast dried, unannealed or "as cast" film ("Fast AC"). These two samples are chosen to provide a contrast between films with a highly ordered and poorly ordered microstructure, respectively. We find that changes in processing not only affect the magnitude of recombination, but also the type.

2. Background

Impedance spectroscopy is an established method for characterizing the electronic properties of dye sensitized and polymer

Dr. J. I. Basham, Dr. D. J. Gundlach
Semiconductor and Dimensional Metrology Division
Physical Measurement Laboratory, NIST
100 Bureau Drive
Gaithersburg, MD 20899–8120, USA
E-mail: david.gundlach@nist.gov
Dr. J. I. Basham, Prof. T. N. Jackson
Department of Electrical Engineering
Penn State University
University Park, PA 16802, USA

DOI: 10.1002/aenm.201400499

© 2014 WILEY-VCH Verlag GmbH & Co. KGaA, Weinheim

solar cells, for which several reviews are available.[22–25] In this technique, a DC offset superimposed with a small AC signal across a wide frequency range are applied across the device. The response spanning many decades of frequency space reveals characteristic response times. The impedance is broken down into its real and imaginary components to discriminate between resistive and capacitive components, and fitted to a representative model circuit where the number, arrangement, and magnitude of the elements are chosen to reproduce the impedance spectrum of the device. The relationship between representative circuit element and real physical processes has been well-described in the literature. A brief review will be given here for convenience. For this work, the impedance spectra of P3HT:$PC_{61}BM$ solar cells were measured and fitted to a model AC equivalent circuit in a fashion similar to the methods of Bisquert and coworkers,[25–28] as shown in **Figure 1**a along with its DC equivalent in Figure 1b. The main difference in this work is that we use a lumped chemical capacitance where others use a distributed capacitance. Because we observe almost no frequency dispersion in the model elements of efficient devices and the time constants for recombination and transport are well-separated, both circuit models arrive at nearly identical results. A lumped capacitance, however, provides a more robust convergence during fitting and was therefore adopted because of this advantage. The circuit contains a series resistance (r_s), due to the substrate and contacts. We find that the fitted value for r_s does not vary with applied voltage and is equal to the resistance measured in an indium tin oxide (ITO)/poly(3,4-ethylenedioxythiophene):polystyrene sulfonate (PEDOT:PSS)/Ca/Al dummy stack comprised of substrate and contact materials only (approximately 3 Ω cm^2). An areal capacitance and area specific resistance (C_t, r_t) represent

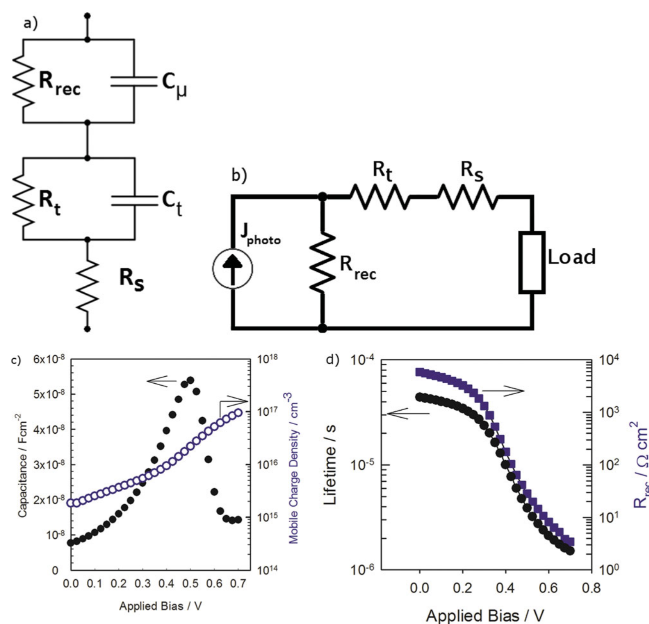

Figure 1. Equivalent circuits diagrams for a) impedance spectroscopy (AC) and b) J–V curve reconstruction (DC) 1c. Magnitude of chemical capacitance C_μ and carrier density n calculated for $\alpha = 0.3$ in the Slow AN device. 1d. The lifetime $\tau(n) = r_{rec} \times C_\mu$ (circles) and recombination resistance r_{rec} (squares) in the Slow AN device.

contact and transport effects.[23,26,28,29] The time constant $\tau_t = C_t r_t$ is characteristic of the time to inject charge into the active layer and transport it across the device. This transport time is easily distinguished from the recombination lifetime as it is 2 to 3 orders of magnitude faster. Most importantly for modeling recombination are the chemical capacitance (C_μ) and recombination resistance (r_{rec}). The chemical capacitance is the increase in charge (Q) and carrier density (n) with a change in the quasi Fermi level (E_f), $C_\mu = q\frac{dQ}{dE_f} = q^2 L \frac{dn}{dE_f}$. It is also closely related to the filling of the density of states.[25] Both C_μ and C_t are corrected for the geometric capacitance parallel to both, C_g, simply approximated by treating the P3HT:$PC_{61}BM$ film as a dielectric with $C_g = \frac{\varepsilon A}{L} = 25$ nF cm^{-2}, where A is the device area and L is the active layer thickness. Because impedance spectroscopy measures the response to an AC signal, the measured capacitance corresponds to the fastest responding carrier. For this material system it is assumed that we measure the electrons in $PC_{61}BM$, since in neat films they have a higher mobility (10^{-3} cm^2 V^{-1} S^{-1})[30] than holes in P3HT (10^{-5} cm^2 V^{-1} S^{-1}).[31] We are also constrained to measuring the mobile charge in the device, as fixed charges will not respond to the AC signal. Because charge is likely transported via hopping given the low mobilities involved, our definition of "mobile" includes localized charges that are able to respond at the measurement frequency, but not carriers which remain deeply trapped for longer than ≈1 ms. By integrating the chemical capacitance across the shift in the quasi Fermi energy, the increase in the concentration of the faster carrier type can be calculated as

$$n = \frac{1}{L}\int C_\mu \, dE_f + n_0 = \frac{1}{qL}\int C_\mu \alpha \, dV + n_0 \quad (1)$$

where C_μ is the chemical capacitance, E_f is the quasi Fermi level, V is the applied potential, q is the elementary charge, and α is a proportionality constant relating the voltage to the shift of the quasi Fermi level for one carrier type. n_0 is the carrier concentration at the lower bound of integration. We begin integrating at $V = 0$ (short circuit) so that n_0 can be approximated as the charge carrier flux at one Sun times the transit time, $\frac{1}{qL} J_{sc} r_t C_t$ resulting in a value of $n_0 = 10^{15}$ cm^{-3}. C_μ and n for the "Slow AN" cell are plotted in Figure 1c. The assumption is made that the contacts are ohmic, and that the applied bias is able to shift the Fermi levels directly in the bias range used, approximately 0 V to 700 mV, just above V_{oc}. While some deviation from a constant relation is expected due to non-ideal Schottky barriers, fixed charge, etc., we find that in this particular range the approximation is adequate in high efficiency cells to produce an accurate model. The open-circuit voltage is the sum of the shifts in electron and hole Fermi levels, $-q\partial V_{oc} = \partial E_{f_n} - \partial E_{f_p}$.[27] Because we measure the applied voltage instead of measuring the quasi Fermi level directly, we scale the voltage in Equation (1) by the factor α to approximate the Fermi level shift for electrons in $PC_{61}BM$. For a symmetric density of states in P3HT and $PC_{61}BM$ one would assume equal shift in each material and a value of 0.5 for α. Because the effective density of states is known to be higher in $PC_{61}BM$ than P3HT it is reasonable to expect less shift of the Fermi level in $PC_{61}BM$ and a value of α less than 0.5. We choose to treat α as a fitting parameter for best agreement between the recombination rate at open

© 2014 WILEY-VCH Verlag GmbH & Co. KGaA, Weinheim

circuit and the generation rate at short circuit, and will later determine a more precise value.

Another important equivalent circuit element, the recombination resistance, models the rate of recombination in the cell. The current which flows through the recombination resistor in the DC equivalent circuit (Figure 1b) is the recombination current. The magnitude is a strong function of bias as a reverse bias causes carriers to be swept out before they have time to recombine, while biasing at open circuit causes all generated carriers to recombine. It is related to the cell's characteristic response time, which is also the mobile carrier lifetime τ by[25,26]

$$\tau(n) = r_{\text{rec}} C_{\mu} \tag{2}$$

τ and r_{rec} for the "Slow AN" cell are plotted in Figure 1d. The lifetime is not constant and will decrease with increasing carrier density. This measure of the mobile carrier lifetime is then used to define the recombination rate (R), using the carrier density from Equation (1) and lifetime from Equation (2):

$$R = \frac{n - n_0}{\tau(n)} \tag{3}$$

where R is the volume averaged increase in recombination rate. Again, we choose n_0 to be the carrier density at short circuit because this will be a small value, and because this choice allows us to use the short circuit current to derive a net generation rate. We prefer this method of quantifying recombination over others, as it does not assume a fixed relation of the recombination rate to carrier density a priori, for example the linear dependence assumed for trap mediated recombination, or the n^2 dependence assumed for Langevin or bimolecular recombination. Simple accounting using the continuity equation gives the result that the J–V curve will be the difference between generation and recombination at each particular bias point,[5]

$$G - R = \frac{-J(V)}{qL} \tag{4}$$

where G, the generation rate is taken for simplicity to be a constant defined as $G = \frac{-J_{sc}}{qL}$. J_{sc} is determine by measuring the current under illumination and 0 V bias using a source-measure unit immediately preceding the impedance measurement. More specifically, G is a measure of the generated charge which is collected at the electrodes, actually being the bottom bound on the generation rate. For efficient cells it has been shown that the internal quantum efficiency is near unity, making this approach a close estimate of the total generation rate.[32] The initial assumption made here is that the generation rate is not field dependent. This can be valid for high quality cells with high fill factors and shunt resistances, though exploration of some systems has suggested that a field-dependent generation rate (or field-assisted extraction) could be responsible for low fill factors.[5–7,33] The modeled J–V curve will have a slightly higher fill factor because of the assumption of field-independent generation, though we observe only a small disagreement, suggesting that this is a valid assumption. Measurement of low performance cells with low shunt resistances have shown generation will be field dependent, to be discussed later. Equation (4) includes the convention that current will be negative at short circuit, introducing a negative sign on the right hand side. Solving for $J(V)$ results in

$$J(V) = -qLG + qLR(V) \tag{5}$$

Because we can easily measure J_{sc} we substitute the approximation $G = \frac{-J_{sc}}{qL}$ into Equation (5) for the more simple expression

$$J(V) = J_{sc} + qLR(V) \tag{6}$$

The DC equivalent circuit embodied in Equation (6) is the same depicted in Figure 1b. The photogenerated charge is embodied by the current source, J_{photo}.

3. Results

In order to correctly scale the magnitude of recombination, we must select an appropriate value of α in Equation (1) to relate the total applied potential to the Fermi potential shift in PCBM only. As a starting point, we assume a symmetric density of states, meaning half of the Fermi level shift is in PCBM and α = 0.5. This yields the blue circles shown in **Figure 2**, and proves to be a slight overestimate of the carrier density. To determine α, we set $J(V_{oc}) = 0$ using Equation (6) and solve for α. This gives a value of $\alpha = 0.3$. Specifically, this value matches the modeled open circuit potential to the measured value by matching the best estimate of the generation rate (from the current at open circuit) to recombination at open circuit where $G = R$. This result indicates that the Fermi level shifts more in P3HT than in PCBM, as expected from the density of states argument made earlier. The modeled J–V curve using $\alpha = 0.3$, shown in Figure 2 ("X" symbols), shows excellent agreement with that measured in the traditional fashion using a source measurement unit (solid line). The predicted fill factor and open-circuit potential match the measured values within about 2%, shown in **Table 1**. The quality of the fit is high, having a coefficient of determination $R^2 = 0.988$.

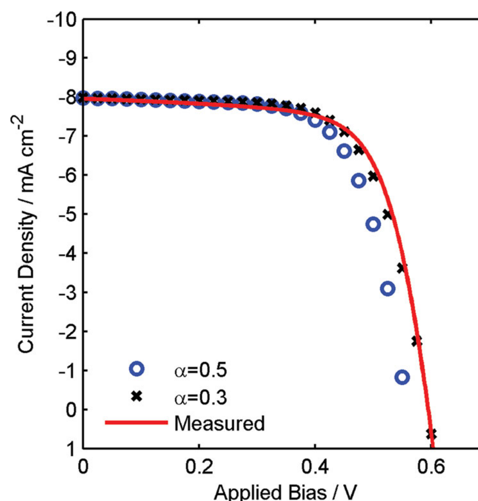

Figure 2. J–V curve reconstruction from Equation (6).

© 2014 WILEY-VCH Verlag GmbH & Co. KGaA, Weinheim

FULL PAPER

Table 1. Values extracted from a measured *J–V* curve vs. those predicted by the model.

	Measured Value Slow AN	Modeled Value Slow AN	Measured Value Fast AC	Modeled Value Fast AC
J_{sc} [mA cm^{-2}]	−7.95		−2.33	
V_{oc} [mV]	594	594	574	574
Fill factor [%]	69.0	67.6	44.8	44.7
Efficiency [%]	3.26	3.20	0.60	0.60

The approximation of field-independent generation works very well in the case of the high efficiency cell modeled in Figure 2. However, morphology plays an important role in charge separation and cells without ideal phase separated morphology can exhibit a strong field dependence of the generation rate. In order to demonstrate this, Fast AC devices were made in a way which caused the P3HT:PC_{61}BM film to dry quickly, resulting in a more finely mixed distribution of P3HT and PC_{61}BM. No annealing was carried out, as this would have served to cause phase separation. All other aspects, including contacts and blend ratio were the same. This film structure is closer to a single mixed phase than the bicontinuous bulk heterojunction present in the first device. Equation (6) overestimates the fill factor because geminate recombination occurs on a time scale too fast to be seen via impedance spectroscopy and is therefore not included in the measured recombination rate. In order to include geminate recombination, we effectively subtract it from the generation rate with a modified form of Equation (6):

$$J(V) = J_{sc}\left(1-\gamma\frac{V}{L}\right)+qLR(V) \tag{7}$$

in which the newly introduced factor γ describes the strength of the field dependence of the generation rate. The quantity V/L is used to approximate the changing electric field as a uniform potential drop across the bulk. This is a convenient definition, although it should be expected that the potential will predominantly drop over a smaller region. This observed relationship could have a few different physical origins. For one the exciton dissociation rate could be linearly dependent on the electric field, causing the rate of geminate recombination to increase as open circuit is approached. We expect the phenomenon responsible for this loss is outside the timescale of the measurement (20 Hz to 2 MHz) or it would be included in the recombination term. A combination of high series and low shunt resistance can lead to a similar change in the shape of the *J–V* curve, however we do not observe a change in the series resistance between the Slow AN and Fast AC devices. The dark current at −1 V reverse bias is below 0.01 mA cm^{-2} for both devices, excluding the possiblity of a true resistive shunt pathway. Using Equation (7) we are able to model the *J–V* curve of the Fast AC device with a more appropriate fill factor, seen in **Figure 3**. When including the factor γ our prediction is again able to match the observed values for fill factor and efficiency almost exactly with α = 0.18 and $\gamma = 7.5 \times 10^{-4}$ cm V^{-1}. The quality of fit is high with R^2 = 0.997 while still maintaining the condition

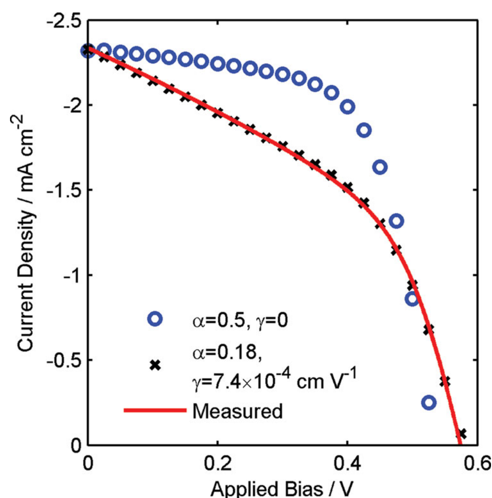

Figure 3. Modeled *J–V* curve for Fast AC device incorporating field-dependent generation.

that the open circuit potentials must match. The large value of γ indicates that charge extraction is heavily dependent on the electric field. At the maximum power point 61% of the current loss is due to the field dependence of charge extraction.

Returning to the Slow AN cell, we include the fitting parameter γ to explore the possibility of geminate recombination in our more efficient device. By freely varying α and γ to minimize error, we find an optimized values of α = 0.27 and $\gamma = 4.6\times10^{-7}$ cm V^{-1}. For comparison, at the max power point of the Slow AN cell only about 2% of the total current loss can be ascribed to the field dependence, suggesting that it is not a determining factor in overall cell performance. It also explains why fitting with Equation (6) which lacks a term for field dependence is still able to produce a good fit.

Determining that recombination in the Slow AN cell must be predominantly non-geminate, we now seek further detail. The recombination rate, shown in **Figure 4**a follows a power law dependence on carrier concentration, $R \propto n^{\delta}$, where delta is the order of recombination.[17,34,35] Insight into the recombination mechanism can be gained from the order of recombination. Generally, an order of 1 implies recombination via deep traps, 2 implies bimolecular recombination, and higher orders imply surface recombination or non-ideal carrier gradients with an extent approaching the active layer thickness.[36] In Figure 4b we plot the local order of recombination using the relation[36]

$$\delta(n) \equiv \frac{d\log(R)}{d\log(n)} \tag{8}$$

In calculating n in the dark, we use the same value of α = 0.3 calculated under illumination and find good agreement between the measured and predicted dark *J–V* curves (not shown). It is interesting to see that there are stark differences between the order of recombination and therefore mechanism of recombination not only between the same cell in the dark and under illumination, but also close to short circuit and close to open circuit. Under illumination, we see that although generation is the same at all points the order of recombination is close to one at short circuit. Carriers are swept out of

 © 2014 WILEY-VCH Verlag GmbH & Co. KGaA, Weinheim

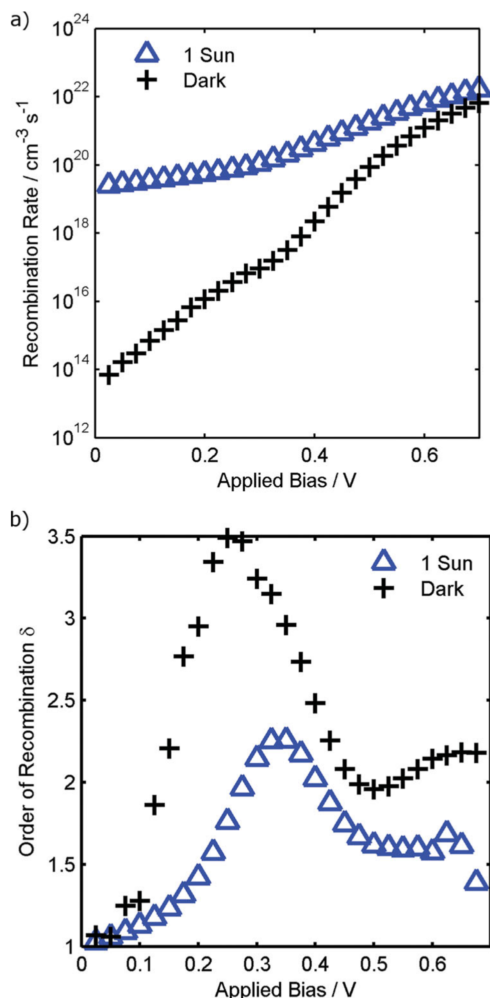

Figure 4. Differences in the Slow AN device in a) recombination rate as a function of applied bias and b) order of recombination as a function of applied bias in the dark and under illumination.

the device quickly and their concentration is low, comparable to the concentration of traps, and trap-mediated recombination is the dominant process. Close to open circuit less current is extracted, raising carrier concentration to the point where carrier density is large compared to the trap state density and bimolecular recombination becomes dominant. Near V_{oc} a value of $\delta = 1.6$ is observed, indicating that both bimolecular and trap-mediated recombination are present under this condition. Applying bias will also modulate the width of the depleted region which affects the apparent order of recombination when measured via Equation (7).[37] Because we use a spatially averaged carrier concentration this effect is not corrected, and can explain the high value of δ seen at about 0.3 V. Device models incorporating spatial inhomogeneity in carrier density show that this effect, especially in cells having a thin active layer, can result in values of δ well over 2.[36] Additionally, a mobility which strongly increases with carrier concentration could yield values of δ above 2 when considering that Langevin recombination carries a mobility dependence, $R = \frac{q}{\varepsilon}\mu_n(n)np$. To fully confirm this possibility would require knowlege of both hole and electron mobilities and concentrations in both phases of the bulk heterojunction, however, as previous Langevin models have shown an effective medium approximation to be invalid. At open circuit where the carrier profiles are nearly homogeneous we measure an order of recombination of $\delta = 1.8$, indicating predominantly bimolecular recombination with some trap mediated recombination, in good agreement with observations of the intensity dependence of the open circuit voltage and charge extraction measurements.[17,38]

To probe further into differences at varying illumination levels, mobility (μ) was measured as a function of illumination intensity (ϕ). We use a transit time based analysis utilizing the time constant extracted from the part of the equivalent circuit related to transport, $\tau_t = r_t \times C_t$:

$$\mu(\Phi) = \frac{L^2}{V_{oc}(\Phi)\tau_t(\Phi)} \tag{9}$$

Here the transit time is measured at short circuit, and V_{oc} represents the open circuit potential at the same illumination level. This would provide an upper limit to the mobility, as the width of the depleted region of the device will be somewhat less than the total device thickness. Mobility is plotted in **Figure 5** for both the high and low efficiency cell. In the high efficiency cell, mobility is initially low but quickly plateaus to a value of 3×10^{-4} cm^2 V^{-1} s^{-1} indicating that there are likely localized, with transport occurring via hopping. In the lower efficiency cells, however, mobility remains low and slowly increases with intensity. This may indicate trapping through states with a broader distribution of activation energies than the more efficient cell. Because the built in field also increases with illumination intensity, we must also consider field-induced barrier lowering for hopping. Because both films are spun from the same solution we can conclude that the differences in mobility are morphological in nature. It is likely that the high efficiency Slow AN cell has larger and more well-ordered domains that provide good percolation pathways to the collecting electrode, while the lower mobility cell will have much greater disorder and small, poorly connected domains.[39,40] If the probability of exciton dissociation is dependent upon mobility, as many interpretations predict, then the generally low mobilities observed

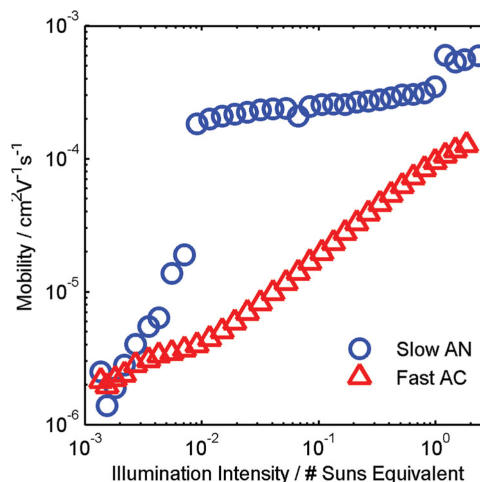

Figure 5. Mobility estimated from Equation (9).

© 2014 WILEY-VCH Verlag GmbH & Co. KGaA, Weinheim

in the low efficiency cell could explain the observation of field-dependent generation.

4. Conclusion

In conclusion this work has demonstrated a method for predicting the *J–V* curve using impedance spectroscopy. The recombination rate is quantified from the characteristic capacitance and resistance of the device. The shape of the *J–V* curve is reproduced with great accuracy because the impedance measurement is performed at nearly identical conditions to the traditional method. To emphasize the importance of this aspect the recombination rate in both the dark and under illumination is shown in Figure 4a. The discrepancy between the two can be as high as a factor of 100 due to the differences in carrier distribution, concentration, type, lifetime, and recombination mechanism mentioned previously. It is important that the method for measuring recombination incorporates the proper bias and illumination conditions, as we have shown that both have a strong effect on the recombination rate and mechanism. Therefore, impedance spectroscopy and the methods outlined in this work are particularly well suited for measuring recombination in a way consistent with Equation (6). The variation we observe with bias and intensity can explain why different methods of measuring recombination arrive at different conclusions: because the devices are not under equivalent testing conditions.[17,41–43]

The *J–V* curve of a high performance cell is modeled with high accuracy while it is noted that poor performing cells are more difficult to model, requiring the inclusion of field-dependent generation. The observations are in excellent agreement with studies using transient photovoltage. The mechanism of recombination is seen to shift from trap-mediated at short circuit to mostly bimolecular near open circuit. We also observed that mobility is lower in fast dried films and slowly increases with intensity. Finally, we show that fast dried films suffer from a very strong field dependence of charge extraction, likely due to geminate recombination, and that proper film processing is key to minimizing recombination losses.

5. Experimental Section

Fabrication: Patterned ITO substrates (Thin Film Devices)[44] were prepared by ultrasonicating in acetone, isopropanol and deionized (DI) water and then dried in an oven. Clean substrates were subjected to UV-ozone treatment for 20 min. PEDOT:PSS (P VP Al 4083, Clevios) was dispensed through a 0.2 μm polypropylene filter and spin coated at 167π rad s^{-1} (5000 rpm). All further fabrication and testing was performed in an argon-filled glovebox. PEDOT:PSS films were annealed at 140 °C for 10 min. P3HT (Plexcore OS 2100, Plextronics) and $PC_{61}BM$ (Nano-C) were dissolved overnight in 1,2 ortho-dichlorobenzene (99.8%, Aldrich) and mixed in a 5:4 w/w P3HT:$PC_{61}BM$ solution having total dissolved solids of 15 mg mL^{-1} (Slow AN) or 30 mg mL^{-1} (Fast AC). Solutions were dispensed though a 0.45 μm PTFE syringe filter and spin coated on the prepared substrates at Slow AN films were spun at 20π rad s^{-1} (600 rpm) for 45 s (5 second ramp up) and then quickly removed and covered with a petri dish while still wet to dry over several minutes. Dry films were then annealed at 140 °C for 10 min. Fast AC films were spun at 40π rad s^{-1} (1200 rpm) for 60 s and were not annealed. Calcium (20 nm) and aluminum (60 nm) were thermally evaporated at a rate of 2 Å s^{-1} from a base pressure of 1.3×10^{-4} Pa (10^{-7} Torr) through a shadow mask. The active area, as defined by overlap of isolated ITO and metal contacts, was 4 mm^2.

Characterization: Current–voltage characteristics were measured using a Keithley 2636A source meter. Illumination was provided by a Newport Oriel xenon arc lamp using AM1.5G filters. An intensity of 100 mW cm^{-2} was set with a calibrated KG filtered silicon diode. The spectral mismatch factor was measured to be 0.99.[45] Impedance spectra were measured in the range of 20 Hz to 2 MHz using an Agilent E4980A LCR meter. A DC bias applied across the anode and cathode was superimposed with a 25 mV AC signal. During the measurement the device was illuminated by a neutral white light-emitting diode (LED; LED Engin). The intensity was set to give the same short circuit current as 1 Sun AM 1.5G illumination for "1 Sun equivalent" conditions. The spectral mismatch was calculated against a KG-filtered diode to be 1.03, for which the intensity was corrected. Impedance spectra were fitted to the circuit model by freely varying all elements except for the geometric capacitance, which was fixed at a constant 25 nF cm^{-2} for a 100 nm thick layer with a relative dielectric constant of 3. This agrees with the measured value of the fully depleted capacitance under –1 V bias in the dark.

Acknowledgements

The authors would like to thank Jason Campbell, Carsten Deibel, Behrang Hamadani, and Lee Richter for helpful discussions.

Received: March 21, 2014
Revised: April 19, 2014
Published online:

[1] F. C. Krebs, N. Espinosa, M. Hösel, R. R. Søndergaard, M. Jørgensen, *Adv. Mater.* **2014**, *26*, 29.
[2] J. You, L. Dou, K. Yoshimura, T. Kato, K. Ohya, T. Moriarty, K. Emery, C.-C. Chen, J. Gao, G. Li, Y. Yang, *Nat. Commun.* **2013**, *4*, 1446.
[3] A. Wagenpfahl, D. Rauh, M. Binder, C. Deibel, V. Dyakonov, *Phys. Rev. B* **2010**, *82*, 115306.
[4] C. G. Shuttle, R. Hamilton, B. C. O'Regan, J. Nelson, J. R. Durrant, *Proc. Natl. Acad. Sci. USA* **2010**, *107*, 16448.
[5] G. F. A. Dibb, T. Kirchartz, D. Credgington, J. R. Durrant, J. Nelson, *J. Phys. Chem. Lett.* **2011**, *2*, 2407.
[6] B. M. Savoie, B. Movaghar, T. J. Marks, M. A. Ratner, *J. Phys. Chem. Lett.* **2013**, *4*, 704.
[7] G. F. A. Dibb, F. C. Jamieson, A. Maurano, J. Nelson, J. R. Durrant, *J. Phys. Chem. Lett.* **2013**, *4*, 803.
[8] P. P. Boix, A. Guerrero, L. F. Marchesi, G. Garcia-Belmonte, J. Bisquert, *Adv. Energy Mater.* **2011**, *1*, 1073.
[9] T. Kirchartz, B. E. Pieters, J. Kirkpatrick, U. Rau, J. Nelson, *Phys. Rev. B* **2011**, *83*, 115209.
[10] M. Soldera, K. Taretto, T. Kirchartz, *Phys. Status Solidi A* **2012**, *209*, 207.
[11] R. C. I. MacKenzie, C. G. Shuttle, M. L. Chabinyc, J. Nelson, *Adv. Energy Mater.* **2012**, *2*, 662.
[12] M. Gluecker, A. Foertig, V. Dyakonov, C. Deibel, *Phys. Status Solidi RRL* **2012**, *6*, 337.
[13] S. R. Raga, F. Fabregat-Santiago, *Phys. Chem. Chem. Phys.* **2013**, *15*, 2328.
[14] F. Fabregat-Santiago, J. Bisquert, E. Palomares, L. Otero, D. Kuang, S. M. Zakeeruddin, M. Gratzel, *J. Phys. Chem. C* **2007**, *111*, 6550.
[15] T. Kirchartz, F. Deledalle, P. S. Tuladhar, J. R. Durrant, J. Nelson, *J. Phys. Chem. Lett.* **2013**, *4*, 2371.

© 2014 WILEY-VCH Verlag GmbH & Co. KGaA, Weinheim

[16] C. Shuttle, B. O'Regan, A. Ballantyne, J. Nelson, D. Bradley, J. Durrant, *Phys. Rev. B* **2008**, *78*, 113201.
[17] C. Deibel, D. Rauh, A. Foertig, *Appl. Phys. Lett.* **2013**, *103*, 043307.
[18] A. Maurano, R. Hamilton, C. G. Shuttle, A. M. Ballantyne, J. Nelson, B. O'Regan, W. Zhang, I. McCulloch, H. Azimi, M. Morana, C. J. Brabec, J. R. Durrant, *Adv. Mater.* **2010**, *22*, 4987.
[19] A. Foertig, J. Rauh, V. Dyakonov, C. Deibel, *Phys. Rev. B* **2012**, *86*, 115302.
[20] A. Baumann, J. Lorrmann, D. Rauh, C. Deibel, V. Dyakonov, *Adv. Mater.* **2012**, *24*, 4381.
[21] S. A. Hawks, F. Deledalle, J. Yao, D. G. Rebois, G. Li, J. Nelson, Y. Yang, T. Kirchartz, J. R. Durrant, *Adv. Energy Mater.* **2013**, *3*, 1201.
[22] T. Ripolles-Sanchis, A. Guerrero, J. Bisquert, G. Garcia-Belmonte, *J. Phys. Chem. C* **2012**, *116*, 16925.
[23] J. Bisquert, F. Fabregat-Santiago, I. Mora-Seró, G. Garcia-Belmonte, S. Giménez, *J. Phys. Chem. C* **2009**, *113*, 17278.
[24] J. Bisquert, G. Garcia-Belmonte, *J. Phys. Chem. Lett.* **2011**, *2*, 1950.
[25] J. Bisquert, F. Fabregat-Santiago, I. Mora-Seró, G. Garcia-Belmonte, E. M. Barea, E. Palomares, *Inorganica Chim. Acta* **2008**, *361*, 684.
[26] G. Garcia-Belmonte, A. Munar, E. M. Barea, J. Bisquert, I. Ugarte, R. Pacios, *Org. Electron.* **2008**, *9*, 847.
[27] G. Garcia-Belmonte, P. P. Boix, J. Bisquert, M. Sessolo, H. J. Bolink, *Sol. Energy Mater. Sol. Cells* **2010**, *94*, 366.
[28] F. Fabregat-Santiago, G. Garcia-Belmonte, I. Mora-Seró, J. Bisquert, *Phys. Chem. Chem. Phys.* **2011**, *13*, 9083.
[29] F. Fabregat-Santiago, J. Bisquert, L. Cevey, P. Chen, M. Wang, S. M. Zakeeruddin, M. Gratzel, *J. Am. Chem. Soc.* **2009**, *131*, 558.
[30] V. D. Mihailetchi, J. K. J. van Duren, P. W. M. Blom, J. C. Hummelen, R. A. J. Janssen, J. M. Kroon, M. T. Rispens, W. J. H. Verhees, M. M. Wienk, *Adv. Funct. Mater.* **2003**, *13*, 43.
[31] M. Giulianini, E. R. Waclawik, J. M. Bell, N. Motta, *J. Appl. Phys.* **2010**, *108*, 014512.
[32] S. H. Park, A. Roy, S. Beaupré, S. Cho, N. Coates, J. S. Moon, D. Moses, M. Leclerc, K. Lee, A. J. Heeger, *Nat. Photonics* **2009**, *3*, 297.
[33] A. Foertig, J. Kniepert, M. Gluecker, T. Brenner, V. Dyakonov, D. Neher, C. Deibel, *Adv. Funct. Mater.* **2014**, *24*, 1306.
[34] I. Montanari, A. F. Nogueira, J. Nelson, J. R. Durrant, C. Winder, M. A. Loi, N. S. Sariciftci, C. Brabec, *Appl. Phys. Lett.* **2002**, *81*, 3001.
[35] T. Offermans, S. C. J. Meskers, R. a. J. Janssen, *J. Chem. Phys.* **2003**, *119*, 10924.
[36] T. Kirchartz, J. Nelson, *Phys. Rev. B* **2012**, *86*, 165201.
[37] L. Koster, E. Smits, V. Mihailetchi, P. Blom, *Phys. Rev. B* **2005**, *72*, 085205.
[38] G.-J. A. H. Wetzelaer, M. Kuik, P. W. M. Blom, *Adv. Energy Mater.* **2012**, *2*, 1232.
[39] B. A. Collins, J. R. Tumbleston, H. Ade, *J. Phys. Chem. Lett.* **2011**, *2*, 3135.
[40] M. Campoy-Quiles, T. Ferenczi, T. Agostinelli, P. G. Etchegoin, Y. Kim, T. D. Anthopoulos, P. N. Stavrinou, D. D. C. Bradley, J. Nelson, *Nat. Mater.* **2008**, *7*, 158.
[41] R. A. Street, *Phys. Rev. B* **2011**, *84*, 075208.
[42] C. Deibel, A. Wagenpfahl, *Phys. Rev. B* **2010**, *82*, 207301.
[43] R. A. Street, *Phys. Rev. B* **2010**, *82*, 207302.
[44] Commercial materials, instruments, and equipment are identified in this paper to specify the experimental procedure as completely as possible. In no case does such identification imply a recommendation or endorsement by the National Institute of Standards.
[45] V. Shrotriya, G. Li, Y. Yao, T. Moriarty, K. Emery, Y. Yang, *Adv. Funct. Mater.* **2006**, *16*, 2016.

© 2014 WILEY-VCH Verlag GmbH & Co. KGaA, Weinheim

On accurate capacitance characterization of organic photovoltaic cells

J. A. Carr[1] and S. Chaudhary[1,2,a)]
[1]Department of Electrical and Computer Engineering, Iowa State University, Ames, Iowa 50011, USA
[2]Department of Materials Science Engineering, Iowa State University, Ames, Iowa 50011, USA

(Received 26 March 2012; accepted 2 May 2012; published online 21 May 2012)

Capacitance measurements, widely used to characterize numerous semiconductor properties, have been recently adopted to characterize organic photovoltaic (OPV) devices. It is known that certain challenges are associated with capacitance measurements. Of upmost importance is the employment of a proper measurement model (series or parallel). Owing to larger capacitive impedances and low series resistances, the parallel model is typically employed in inorganics. However, we find that for characteristically thinner organic films, a hybrid model should be used. We highlight the inconsistencies in OPV literature due to indiscriminate usage of parallel model and show how proper model selection can rectify any artifacts. © *2012 American Institute of Physics*. [http://dx.doi.org/10.1063/1.4720403]

Capacitance spectroscopy has been employed to study semiconductor properties for many years. Recently, these techniques have been adopted by the organic photovoltaic (PV) community to probe device aspects such as doping density,[1–3] deep trap states,[4–6] carrier mobility,[3] and active layer thickness.[7] It is well understood that these measurements can be very sensitive and are plagued by issues such as high impedances, leaky capacitances, and noisy cabling. Of upmost importance in maintaining reliable measurements is the selection of the proper model (e.g., parallel, series, or multiple parameters) during the measurement process. A conventional measurement employs the equivalent circuit shown in Fig. 1(a), where R_s represents the series resistance, R_p the parallel resistance, and C the capacitance. With three unknowns, measurements must be taken at two frequencies, and complex equations must be solved to find the capacitance and its associated resistances; see Ref. 8 for example. For simplicity, this equivalent circuit can be accurately modeled by either the series (highlighted by blue, solid box) or parallel (highlighted by red, dashed box) segment, depending on which portion dominates as per the capacitance, resistances, frequency, etc. In a typical solar cell, the series resistance is expected to be quite small and the parallel resistance quite large. Therefore, for large capacitive impedances, the parallel portion overshadows that of the series and dominates the measurements. In this case, the parallel model gives an accurate approximation of the equivalent circuit. In contrast, as the magnitude of capacitive impedance approaches that of the series resistance, the series model gives the most accurate approximation. Within the inorganic community, parallel parameters are typically employed. Owing to smaller series resistances and larger capacitive impedances, this parallel model remains accurate over the usual frequencies employed (e.g., 10 Hz–2 MHz). In this report, we show this detail is not directly transferrable to organic PV cells—the parallel parameters cannot be indiscriminately used. When comparing organic and inorganic cells with similar contact area, our data shows series resistances are typically two or more times higher and capacitive impedances three or more times lower in the organic devices. This moves the transition from the parallel model to the series model to lower frequencies—which can be within the range of interest. Thus, a hybrid of the two models must be employed to accurately measure the capacitance over the frequency range of interest. We show, if the improper parameters are used, geometric capacitances are underestimated, deep trap states are overestimated, and general conclusions are greatly misinterpreted. Although model choice may be a known concept, we find several evidences of improper model usage within the organic PV literature and highlight the inaccuracies they create.

As an initial example, we first turn to the capacitance versus frequency (CF) measurement of a Phenyl-C_{61}-butyric acid methyl ester (PCBM) only device (characterization details can be found in the supplementary material[15]). PCBM is a fullerene derivative of the C_{60} (or C_{70}) buckyball that shows no Mott-Schottky (MS) or deep-trap capacitive behavior with indium tin oxide (ITO) and aluminum contacts.[4] Thus, a flat capacitive response with respect to frequency and voltage is expected. This response represents a geometric capacitance, $C_g = \epsilon A/t$ ($\epsilon \equiv$ the permittivity, $A \equiv$ contact area, and $t \equiv$ thickness), in which only the dielectric is contributing. Fig. 1(b) displays the CF spectra of one such device. One immediately notes the geometric capacitance (horizontal gray at ca. 6.5×10^{15} 1/F^2 according measured thickness of ca. 35 nm, $A = 0.1256$ cm^2 and $\epsilon = 3.9$) requires both models to be accurately represented between 100 Hz and 1 MHz—a typical frequency range of interest as it reaches from near the Fermi level[9] to above the deep trap profile.[4,5] For those frequencies below 7.5 kHz, the parallel parameters gave the best measurement as high impedances of the parallel portion of the circuit overshadow that of the series component and dominate the voltage divider. Between 7.5 kHz and 100 kHz both models gave a good approximation, differing by less than 1%. At frequencies above 100 kHz the series model gave the best approximation. At these frequencies, the parallel impedance-combination of R_p and C falls rapidly owing to the lowering of the capacitive impedance. As this impedance becomes comparable with R_s, the series resistance becomes significant and can no longer

a)Author to whom correspondence should be addressed. Electronic mail: sumitc@iastate.edu. Tel.: 515 294 0606.

 © 2012 American Institute of Physics

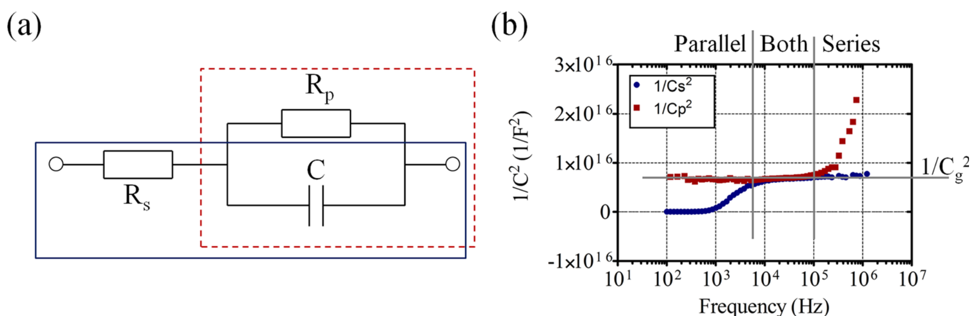

FIG. 1. (a) Simple equivalent circuit for small signal measurements. Any lead inductance is neglected here. The series approximation is highlighted by a solid blue box and the parallel by a dashed red box. (b) Capacitance ($1/C^2$) versus frequency characteristics of a PCBM only device. Both C_s and C_p parameters are shown. The calculated geometric capacitance ($1/C_g^2$) is highlighted by a gray line.

be ignored. The large parallel resistance, however, acts as a current divider and, with sufficiently small capacitive impedances, can be neglected. We note the typically thin active layer of organic films (ca. 100–200 nm) gives a larger capacitance, which causes this transition from the parallel to series to emerge at much lower frequencies than their inorganic counterparts. Frequencies below 100 Hz gave dissipation factors as high as ca. 50, indicating a very leaky capacitor whose measurement is most likely overwhelmed by noise. Above 2 MHz it is expected that the series model will continue to dominate. The PCBM device data illustrates the notion that indiscriminately using a parallel approximation across the spectrum does not transfer to organics.

The above directly translates to bulk heterojunction (BHJ) devices comprising a 1:1 weight ratio of poly(3-hexylthiophene) (P3HT):PCBM. Device fabrication details can be found in the supplementary material.[15] Fig. 2(a) plots C versus F for one such device. A pattern similar to the PCBM only device emerges, where lower frequencies favor the parallel approximation, higher frequencies favor the series, and those in-between can be estimated by either. One notes the parallel model still gives relatively reasonable values at higher frequencies. However, these values differ from the series model by anywhere between 1 and nearly 200% for this device. The choice of which of these models is most accurate is convoluted by the fact that, unlike PCBM only devices, the polymer adds a doping and deep-trap profile.[2,4,5,10] Thus, the expected capacitance may be unknown. However, at sufficiently high frequencies, the demarcation energy at which neither mobile charges nor trap states respond can be surpassed, and only the dielectric contributes to the capacitance. Thus, the geometric capacitance should be expected. We found this frequency experimentally to be ca. 1.5 to 2 MHz depending on the particular device. Qualitatively, the energy corresponding to this frequency range makes sense as it is nearing or slightly less than the equilibrium Fermi-level of P3HT (ca. 0.33 eV with doping ca. 1×10^{16}–$1 \times 10^{17}\,\mathrm{cm}^{-3}$ as determined by 1 MHz capacitance versus voltage (CV) analysis[11]). We further confirm this geometric capacitance by applying a large (−2 VDC) reverse bias along with the entire small-signal frequency spectra in order to fully deplete the active layer—the same C_g was obtained for all frequencies at −2 VDC. Keeping this geometric capacitance in mind, the series model gave the most accurate approximation above 1.5 MHz. Further, we note that only the series capacitance reaches a plateau at these frequencies, while the parallel capacitance continues to drop. Extrapolating back, this indicates that the series model should be used for all frequencies greater than 11 kHz in these particular devices. This has two main implications for common applications of capacitance measurements: (i) C_g and thickness measurements, and (ii) determination of deep trap profiles. Both will be discussed in detail later in this report.

Of course, the boundaries at which the model must change are highly dependent on the device. Smaller capacitances, as well as series resistances, can push the parallel to series transition into higher frequencies. With a sufficiently low capacitance and R_s combination, the change may not even be noticed within the define frequency range, as is typically the case with silicon cells. A well known technique for monitoring model choice is to track the magnitude of the impedance.[12] Fig. 2(b) shows the magnitude of impedance versus frequency for the 1:1 BHJ device studied in Fig. 2(a). The general guidelines which are typically used are (i) the parallel approximation for $|Z| > 10\,\mathrm{k\Omega}$, the series approximation for $|Z| < 1\,\mathrm{k\Omega}$, and either for $1\,\mathrm{k\Omega} < |Z| < 10\,\mathrm{k\Omega}$. Fig. 2(b) shows good agreement with these guidelines.

We next turn to the literature and some of our own data to highlight inconsistencies generated by improper model usage. These inconsistencies seem to have led and, in the future, may lead to incorrect data, misinterpreted conclusions, or both. In a recent report by Li *et al.*, capacitance

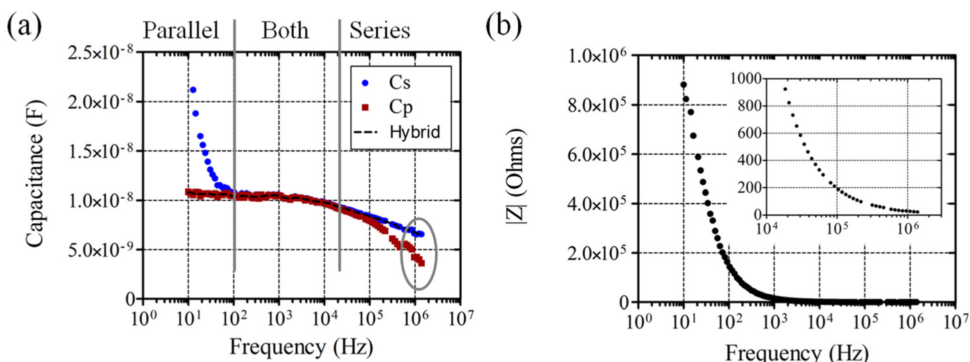

FIG. 2. (a) Capacitance versus frequency characteristics of a typical P3HT:PCBM (1:1) BHJ PV device. The ellipse highlights the differences in the geometric capacitance obtained by each model. (b) Impedance versus frequency plots showing an exponential decrease in the impedance magnitude. The inset magnifies the 10 kHz–1.5 MHz regime where |Z| drops below 1 kΩ.

techniques were used to simultaneously measure carrier density and mobility in organic semiconductors.[3] Although we generally agree with their method, we find inconsistencies in the measured geometric capacitance and the conclusions directly drawn from it. In the report, P3HT only films were characterized by CV method (−3.0 V to +0.5 V) at different frequencies (100 Hz–1 MHz). The authors found that at frequencies of 10 kHz and above, the film did not exhibit a MS response. This indicates that 10 kHz is the boundary above which mobile charges as well as trap states cannot respond, and only the geometric capacitance is measured. From this, one is left to draw the conclusion that CV and other capacitance measurements (CF, deep-level transient spectroscopy, etc.) should be conducted at frequencies lower than 10 kHz. Qualitatively, this conclusion seems implausible as the demarcation energy of 10 kHz is ca. 0.477 eV ($E_\omega = E–E_{HOMO} = kT\ln(\omega_0/\omega)$[13] with ω_0 estimated at $1 \times 10^{12}\,s^{-1}$), which is nearly 0.1 eV above the Gaussian center of the deep trap profile in P3HT films.[4,5] Thus, at 10 kHz, one would expect these lower lying trap states and mobile charges to respond.[11] Further, our data does not support this 10 kHz conclusion as we see MS behavior for frequencies as high as 1 MHz on P3HT only devices. As a possible explanation for this discrepancy, we explored the differences between the series and parallel approximations for CV data between 100 Hz and 1 MHz. As shown in Fig. 3(a), the models give an indication of much different device behavior at 1 MHz on our cells, with the series approximation showing MS behavior and parallel showing only a dielectric response. Here, the impedance magnitude indicates that the series model is more

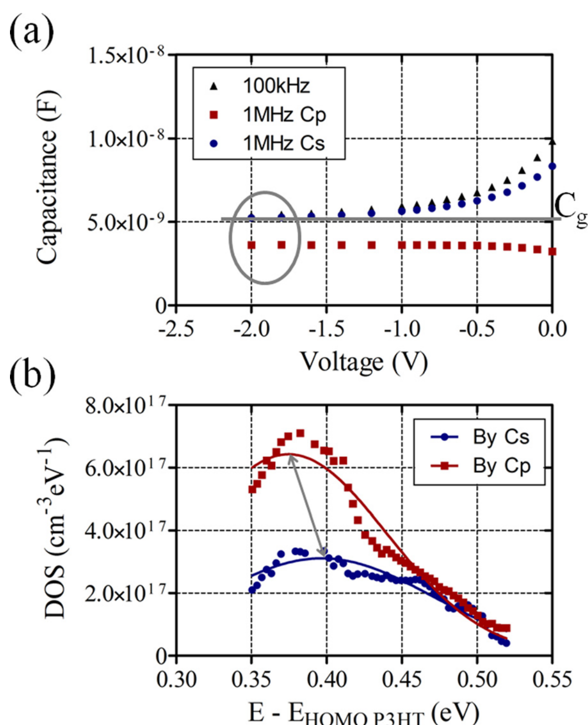

FIG. 3. (a) Capacitance versus voltage characteristics for P3HT only device at 100 kHz and 1 MHz. The calculated geometric capacitance (C_g) is highlighted by the horizontal line. The differences in the geometric capacitance obtained by the models are shown within the circle. (b) Density of trap states versus demarcation energy for P3HT:PCBM (1:1) device. The arrow shows the shift in the Gaussian amplitude and central energy between the two models.

accurate. We note this particular P3HT device did not show low impedances (i.e., <1 kΩ) until ca. 300 kHz owing to a slightly smaller capacitance than that of the referenced work. As further evidence that the parallel parameters give an incorrect depiction of device behavior, we turn to the reverse bias region (−2 VDC). Here, the layer is fully depleted, and we clearly see the parallel model underestimates the geometric capacitance by ca. 250%. Thus, Fig. 2 shows that, for a typical P3HT device, frequencies as high as 1 MHz may still be valid for capacitance spectroscopy, and the currently published 10 kHz data is most likely the result of model misinterpretation. The exact uppermost usable frequency will be dependent on the material's Fermi level and thus can change from device to device. P3HT doping has been reported in the range of 10^{15}–$10^{17}\,cm^{-3}$, from which the Fermi level can be estimated to sit at 0.36 eV above the valence band or lower. This corresponds to freeze out frequencies of ca. 900 kHz or higher. Even doping profiles as low as $10^{14}\,cm^{-3}$ still give a Fermi level of ca. 0.42 eV or a ca. 100 kHz upper frequency. The above finding has further implications for the method of measuring capacitance to find active layer thickness. We have seen the improper model can underestimate C_g by as much as 300%. As a result, thickness can be significantly overestimated if the model is not properly adjusted.

Next, we look at the determination of deep-trap density of states (dTDOS) in organic cells. This method, which is detailed elsewhere,[4] combines CV with CF characterization to sweep through the bandgap and map defects states. As previously highlighted, the series model gives the best approximation for 1:1 BHJ based devices at higher frequencies (10 kHz to 2 MHz). The demarcation energies of these higher frequencies range from 0.477 eV to 0.339 eV. One immediately notes that this is over the range of the reported Gaussian deep-defect profile.[4,5] By comparing these models in Fig. 2(a), a large difference in slope is readily apparent. Thus, as highlighted in Fig. 3(b), if the improper model is employed, the dTDOS magnitude and distribution center can be over- and under-estimated, respectively. Using the parallel approximation, we find N_t to be overestimated by ca. 110% and the central energy to be underestimated by about 20 meV.

Lastly, we investigate a 2008 report by Jarosz.[14] In this report, the author casts doubts on MS analysis of organic planar heterojunction cells. Although we do not question the report in its entirety, we review a single plot displaying C versus F as a function of reverse bias. Here, the author correctly expects the measured frequency-dependent capacitance to decrease with an applied reverse bias. More generally stated, as the reverse bias is increased, the active-layer begins to deplete, and the capacitance at all frequencies decreases to approach the geometric capacitance. The report, however, finds an increase in capacitance with reverse bias for frequencies less than ca. 400 Hz and draws doubts on MS analysis in their cells. Although we cannot state whether MS analysis is valid or not on Jarosz's planar cells, we can highlight how improper model employment could cause one to incorrectly reach the same conclusion—even on P3HT:PCBM BHJ cells. Fig. 4 shows 1:1 BHJ CF analysis as a function of applied DC reverse bias for both the series (Fig. 4(a)) and parallel (Fig. 4(b)) models. The series model

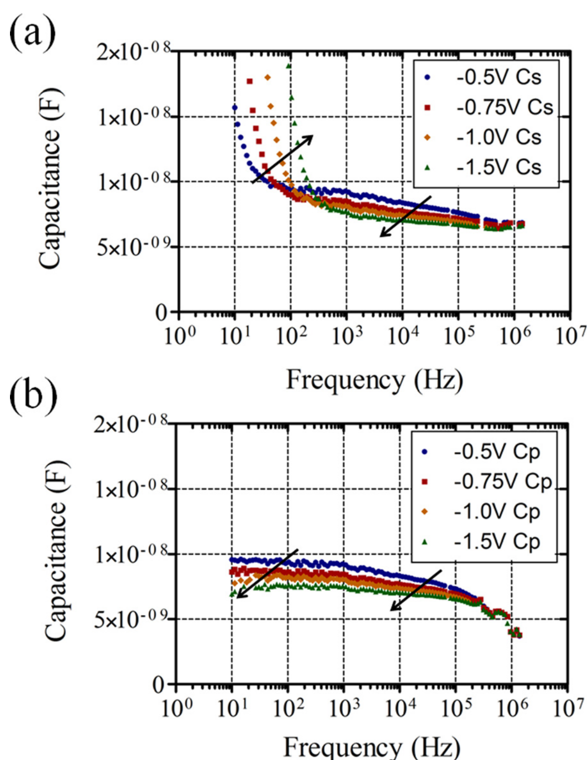

FIG. 4. Capacitance versus frequency as a function of reverse bias for (a) the series model and (b) the parallel model. The arrows indicate the direction of increasing reverse bias.

closely represents the data of the aforementioned report. This artifact arises as a direct result of the series approximation. As frequency decreases, the capacitance impedance increases and the parallel portion of circuit Fig. 1(b) dominates. By continuing to monitor the series portion, the true capacitance measurement is lost. The parallel model removes this artifact and gives the expected response. Hence, by monitoring only the series model, one might reach improper conclusions owing to inaccurate data.

Herein, the capacitance model choice was reviewed in an effort to improve capacitance measurements on organic PV cells. Although series versus parallel model selection may be a known issue, we find evidences in the literature that it is being overlooked within the organic PV community. Owing to higher series resistances and lower capacitance impedances, we find the parallel approximation cannot be indiscriminately used over the frequency range of interest. Most importantly, we find improper model employment can cause discrepancies in the geometric capacitance by as much as 300%, discrepancies in the TDOS by as much as 110%, and, more in general, misinterpreted conclusions. Our work shows that while performing capacitance characterization, it is critical to monitor the impedance magnitude and correspondingly employ the appropriate capacitive circuit model.

We thank Iowa Power Fund from the State of Iowa's Office of Energy Independence, and National Science Foundation (Award No. ECCS–1055930) for financial support. We thank Mehran Samiee Esfahani for providing us with sample silicon PV capacitance data and for helpful conversations.

[1]A. B. Guvenc, E. Yengel, G. Wang, C. S. Ozkan, and M. Ozkan, Appl. Phys. Lett. **96**, 143301 (2010).
[2]G. Dennler, C. Lungenschmied, N. S. Sariciftci, R. Schwödiauer, S. Bauer, and H. Reiss, Appl. Phys. Lett. **87**, 163501 (2005).
[3]J. V. Li, A. M. Nardes, Z. Liang, S. E. Shaheen, B. A. Gregg, and D. H. Levi, Org. Electron. **12**, 1879–1885 (2011).
[4]P. P. Boix, G. Garcia-Belmonte, U. Munecas, M. Neophytou, C. Waldauf, and R. Pacios, Appl. Phys. Lett. **95**, 233302 (2009).
[5]K. S. Nalwa, R. C. Mahadevapuram, and S. Chaudhary, Appl. Phys. Lett. **98**, 093306 (2011).
[6]A. Sharma, P. Kumar, B. Singh, S. R. Chaudhuri, and S. Ghosh, Appl. Phys. Lett. **99**, 023301 (2011).
[7]C. Lungenschmied, S. Bauer, R. Schwodiauer, S. Rodman, D. Fournier, G. Dennler, and C. J. Brabec, J. Appl. Phys. **109**, 044503 (2011).
[8]K. J. Yang and C. Hu, IEEE Trans. Electron Devices **46**, 1500 (1999).
[9]M. J. Deen, M. H. Kazemeini, Y. M. Haddara, J. Yu, G. Vamvounis, S. Holdcroft, and W. Woods, IEEE Trans. Electron Devices **51**, 1892 (2004).
[10]M. S. A. Abdou, F. P. Orfino, Y. Son, and S. Holdcroft, J. Am. Chem. Soc. **119**, 4518 (1997).
[11]L. Kimerling, J. Appl. Phys. **45**, 1839 (1974).
[12]*Agilent Impedance Measurement Handbook, 4th edition* (Agilent Technologies, 2009).
[13]S. S. Hegedus and W. N. Shafarman, Prog. Photovoltaics **12**, 155 (2004).
[14]G. Jarosz, J. Non-Cryst. Solids **354**, 4338 (2008).
[15]See supplementary material at http://dx.doi.org/10.1063/1.4720403 for characterization details and for device fabrication details.

ELSEVIER

Solar Energy Materials & Solar Cells 67 (2001) 323–329

Solar Energy Materials & Solar Cells

www.elsevier.com/locate/solmat

Structure analysis of CIGS solar cells by CV characteristics under monochromatic light at low-temperature levels

T. Koyanagi[a,*], T. Kojima[a], K. Nakamura[a], T. Yanagisawa[a], K. Takahisa[a], T. Negami[b]

[a]*Electrotechnical Laboratory, Device Functions Section, 1-1-4 Umezono, Tsukuba, Ibaraki 305, Japan*
[b]*Matsushita Electric Industrial Co. Ltd., Japan*

Abstract

CIGS solar cells are studied with CV/MCV measurements in a wide range of temperatures. Using a simple model, we succeeded in obtaining shallow trap levels in the bulk from the value of reduction of depletion region width by monochromatic light of proper wavelength. The MCV characteristics are powerful methods to analyze the parameters of multi-layer light-sensitive devices as CIGS solar cells. © 2001 Published by Elsevier Science B.V. All rights reserved.

Keywords: $CuInSe_2$; CV characteristics; MCV characteristics; Solar cell; Series connected capacitance model

1. Introduction

We have studied CIGS solar cells using CV or CF characteristics with or without monochromatic light to check the change of defects in them [1,2].

As we discussed [2], MCV(CV measurement under monochromatic light) is a powerful method to study parameters in semiconductor along its depth because light of different wavelength has different penetration depth. Hitherto our experiments have been done in room temperature to discuss deep level defects in the CIGS solar cells. In this paper, we extended the temperature range lower level to 50 K. At first, we discuss the shift of capacitance value under dark condition during CV measurements

* Corresponding author.

0927-0248/01/$-see front matter © 2001 Published by Elsevier Science B.V. All rights reserved.
PII: S0927-0248(00)00298-1

caused by time and temperature. After that we analyze CV/MCV data for the samples in lower temperature range to obtain short-term trap level around the depletion region in the samples.

2. Experimental

CV characteristics of CIGS solar cells are taken with/without monochromatic light in wide temperature range between 50 and 300 K.

Samples: The CIGS solar cells have the structure of ITO/ZnO/CdS/CIGS/Mo/glass (Fig. 1) which are made by Matsushita Electric Industrial Co. Ltd. [3].

Each sample was measured with four probes and short circuited before and after CV/MCV measurements. Their parameters are shown in Table 1 in order of Ga density in CIGS layer.

Devices: The devices for CV/MCV measurements are HP4192A and monochromatic light source SM-5 of BUNKO KEIKI which were GPIB controlled by a computer. The temperature of the samples was controlled by CRYO KELVIN of DAIKIN controlled through RS-232C cable.

In the measurements, ground wiring is very important to minimize noise, because the cable length between HP4192A and the cryostat is much longer than usual.

Parameters for the measurement are as follows:

Temperature: 50–300 K (50 K step). Temperature can be changed about 3 K/min.

Wavelength: 1100–300 nm (100 nm step). Each MCV measurement is preceded by CV(dark) measurement to check the effect of each monochromatic light.

Voltage: 0–IV (0.05 V step).

Frequency: fixed to 100 kHz to minimize the noise and the induction effect of the cables.

As the measurement procedure, these parameters were swept in the order mentioned above. Each sample had four terminal connections which are short circuited before and after CV/MCV measurements.

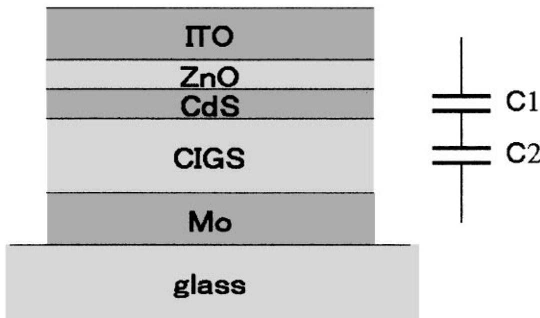

Fig. 1. Structure of samples.

Table 1
CIGS solar cells

No.	Eff (%)	J_{sc} (mA/SC)	V_{oc} (V)	FF	Ga density	Comment
2	14.2	34.0	0.631	0.661	0.170	
3	10.8	32.8	0.638	0.516	0.196	
4	14.0	32.8	0.636	0.670	0.219	
5	13.4	32.2	0.612	0.680	0.228	
7	14.0	33.2	0.612	0.692	0.246	
8	13.9	32.0	0.629	0.689	0.252	
9	13.9	30.9	0.642	0.699	0.258	
10	13.2	33.6	0.609	0.643	0.262	2.5 μm thick
12	13.8	30.8	0.644	0.699	0.273	AR coating
13	14.3	30.2	0.647	0.734	0.294	AR coating
15	13.0	31.3	0.612	0.682	0.348	3 μm thick
16	11.1	29.6	0.608	0.618	0.380	3 μm thick

3. Results

To remove the effect of monochromatic light intensity of xenon lamp in the light source, differences between values changed during CV and MCV measurements were normalized by photon number at each wavelength to give the values for 10–15 photons.

The values of phase angles θ in CV/MCV measurements were checked to be within the order of 0.1 rad in most cases.

3.1. Δw_d vs. wavelength

The values of capacitance obtained from MCV/CV measurements are denoted as C_{light} and C_{dark}. C_{light} is a short-term variable and shows small increase compared to C_{dark}.

The deviation between their reciprocal values is expressed as follows:

$$\Delta(1/C) = 1/C_{dark} - 1/C_{light}. \tag{1}$$

Here $1/C_{dark}$ and $1/C_{light}$ are proportional to the sum of the ith layer thickness divided by (εiS) where εi and S are the dielectric coefficient of the ith layer and the area of the sample.

If the layers except CIGS layer are fixed under monochromatic light of proper wavelength, $\Delta(1/C)$ is proportional to the reduction of depletion width in CIGS layer by the monochromatic light which is denoted as ΔW_d. So the value of ΔW_d is given as

$$\Delta W_d = (\varepsilon S)\,\Delta(1/C), \tag{2}$$

where ε is the dielectric coefficient for CIGS layer.

Fig. 2 shows typical curves for ΔW_d vs. monochromatic wavelength at several temperature levels. Here bias voltage is fixed to a non-zero value ($-$ 0.2 V) because the capacitance at 0 bias often shows abnormal behavior.

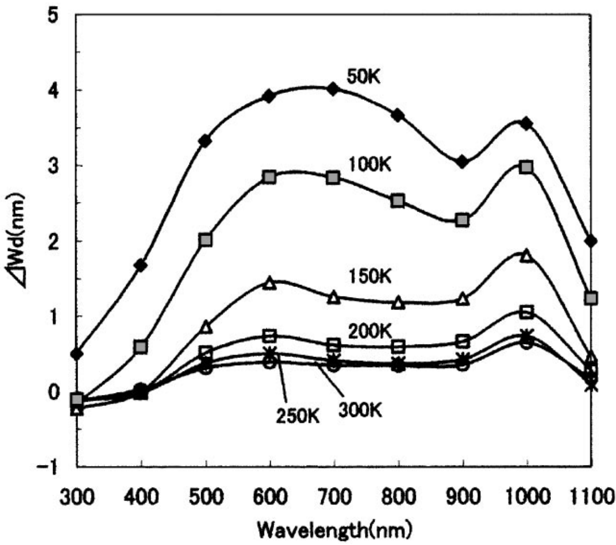

Fig. 2. ΔW vs. wavelength.

3.2. Δw_{d} vs. temperature

Fig. 3 shows the example curves for ΔW_{d} vs. $(1/T)$.

Lines for monochromatic light of various wavelengths show parallel lines in low-temperature range whose slopes give the value of shallow trap levels around the depletion region in the samples.

4. Discussion

4.1. Shift of c_{dark} during the measurement

During the CV/MCV measurement, we found the shift of the C_{dark} value by bias voltage and temperature. These two phenomena are explained as follows:

(1) C_{dark} shift by bias voltage. We have already discussed it [2]. It is caused by a long-term phenomenon to charge-up defects or traps with long-time constant by reverse bias during CV/MCV measurements.

(2) C_{dark} shift by temperature. To make the discussion simple, we approximate the depletion width W for one-sided abrupt junction by

$$W = \mathrm{SQRT}(2\varepsilon V_{\mathrm{b}}/qN), \tag{3}$$

where V_{b} is the built-in voltage. The impurity density N is given as a function of temperature as follows:

$$N = N_0 \exp(-qV_{\mathrm{b}}/kT). \tag{4}$$

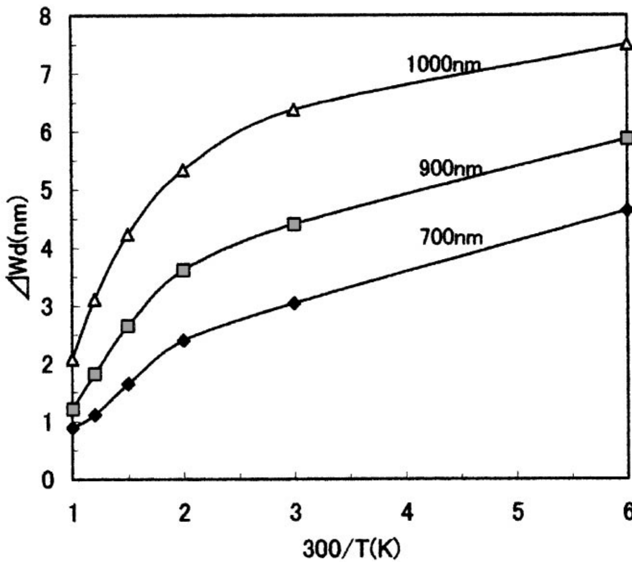

Fig. 3. ΔW vs. temperature.

The value of C_{dark} can be given as follows:

$$C_{\text{dark}} = S\varepsilon/W = S\,\text{SQRT}(q\varepsilon N_0/2V_\text{b})\exp(-qV_\text{b}/2kT). \tag{5}$$

Therefore the value of C_{dark} increases with temperature.

4.2. Δw_d vs. temperature

In Fig. 2, we find two features common to all samples except #15 and #16 whose values of thickness are much larger than those of other samples.

The first feature is that the ΔW_d curve has some valleys in the wavelength range between 700 and 900 nm for higher temperature. The reason is explained as follows.

The monochromatic light in this wavelength range has a proper absorption coefficient which allows the light to penetrate to the depletion region and to be considerably absorbed in the region. The light absorbed in the region generates carriers in it, but the carriers generated are quickly swept outside the region by the strong electric field in it. So the light in this wavelength region contributes little to the value of ΔW_d. This is the reason why curves for higher temperature in Fig. 2 have the valleys.

The second feature is that the ΔW_d curve has some peaks in the same wavelength range as mentioned above. This seems to be the result of growth of the ΔW_d value by temperature reduction. To explain these phenomena, we use a shallow trap model in the bulk. In the model we assume that shallow traps with energy level E_w exist in the CIGS layer.

The occupation probability for those traps is given as follows:

$$p = 1 - \exp(-qE_w/kT). \quad (6)$$

At higher temperature carriers generated by monochromatic light are trapped by them but can easily escape because the occupation probability given as Eq. (6) is small at higher temperature. But if the temperature goes down, trapped carriers cannot escape so easily and form an additional space charge region to that formed by ionized impurity. Thus the trapped carriers at low temperature increase the impurity density in appearances and reduce the depletion width.

As a result, the reduction of depletion width by light denoted as ΔW_d grows by temperature reduction.

4.3. Depth of well-type trap obtained from the Δw_d vs. $(1/T)$ relation

When monochromatic light illuminates the sample, it penetrates into CIGS layer of p-type and will make two types of space charge in depletion region. The first type is made of occupied traps as mentioned above and the second type is made of ionized impurities by the light. Both of them form an additional space charge around the depletion region during light illumination and take the place of ionized impurities by reverse bias voltage. In this paper we neglect the second type of space charge and calculate E_w from Eq. (6) using data for two temperature points 50 and 100 K assuming that ΔW_d is proportional to the value of occupation probability in Eq. (6).

Fig. 4 shows the trap level E_w calculated from data at 700 nm and the peak values for ΔW_d vs. Ga density in the bulk.

From these curves we can note a rough linearity between ΔW_d, E_w and Ga density of the samples. As we mentioned before, samples #15 and #16 have large CIGS thicknesses. The abnormal data obtained for them is the result of this.

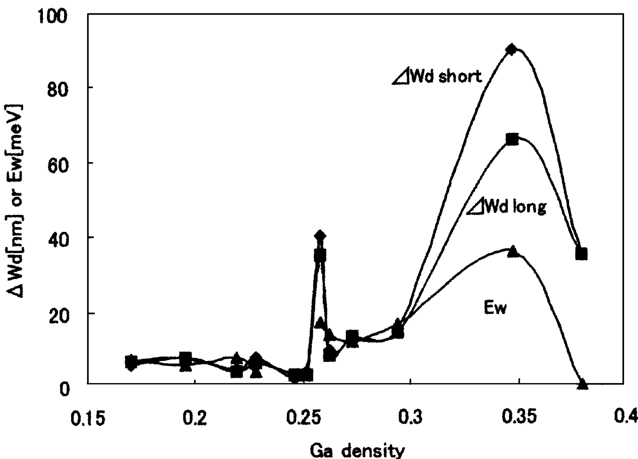

Fig. 4. Parameters vs. Ga density.

5. Conclusions

We applied CV/MCV measurements to CIGS solar cells to study the state in the bulk. Using a simple model, we succeeded in obtaining shallow trap levels in the bulk from the value of reduction of depletion region width by monochromatic light of proper wavelength.

Thus MCV measurement is a powerful technique to check the characteristics of the bulk of semiconductor in various depths, such as shallow trap levels and impurity density in the bulk if the bias, wavelength of monochromatic light and the temperature are properly selected.

Acknowledgements

This work was supported by the NEDO as a part of the New Sunshine Program of the MITI, Japan.

References

[1] T. Kojima et al., Solar Energy Mater. Solar Cells 50 (1998) 87–95.
[2] T. Koyanagi et al., Defect in CIGS solar cells studied with $C(t)$, C–V, C–F and photo spectral characteristics, Proceeding of the Second WCPEC Vienna, 1998, pp. 1121–1124.
[3] T. Negami et al., Effect of absorber thickness on performance of Cu(In,Ga)Se_2 Solar Cells, Proceeding of the Second WCPEC Vienna, 1998, pp. 1181–1184.